

Title	Intrapartum fetal death and doctors; A qualitative exploration
Authors	McNamara, Karen;Meaney, Sarah;O'Donoghue, Keelin
Publication date	2018
Original Citation	McNamara, K., Meaney, S. and O'Donoghue, K. (2018) 'Intrapartum fetal death and doctors; A qualitative exploration', Acta Obstetricia Et Gynecologica Scandinavica, In Press, doi:10.1111/aogs.13354
Type of publication	Article (peer-reviewed)
Link to publisher's version	https://obgyn.onlinelibrary.wiley.com/doi/abs/10.1111/aogs.13354 - 10.1111/aogs.13354
Rights	© This article is protected by copyright. All rights reserved. This is the peer reviewed version of the following article: McNamara, K., Meaney, S. and O'Donoghue, K. (2018), Intrapartum fetal death and doctors; A qualitative exploration. Acta Obstet Gynecol Scand. Accepted Author Manuscript., which has been published in final form at https://doi.org/10.1111/aogs.13354 . This article may be used for non-commercial purposes in accordance with Wiley Terms and Conditions for Self-Archiving.
Download date	2024-04-20 07:31:17
Item downloaded from	https://hdl.handle.net/10468/5771



UCC

University College Cork, Ireland
Coláiste na hOllscoile Corcaigh

Opto-electro-thermal optimization of photonic probes for optogenetic neural stimulation

Na Dong¹, Rolando Berlinguer-Palmini², Ahmed Soltan³, Nikhil Ponon³, Anthony O'Neil³, Andrew Traveyan², Pleun Maaskant⁴, Patrick Degenaar^{3,2}, and Xiaohan Sun^{*,1}

¹ National Research Center for Optical Sensing/Communications Integrated Networking, Dept. of Electronics Engineering, Southeast University, Nanjing 210096, China

² Institute of Neuroscience, University of Newcastle upon Tyne, Newcastle, NE1 7RU, United Kingdom

³ School of Engineering, University of Newcastle upon Tyne, Newcastle, NE1 7RU, United Kingdom

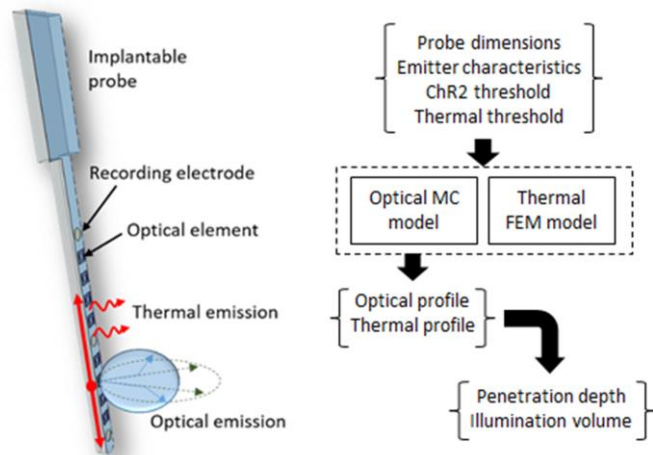
⁴ Tyndall Institute, University College Cork, Ireland

Received zzz, revised zzz, accepted zzz

Published online zzz

Keywords: optogenetics, optrode, optoelectronics, neuroprosthesis, brain implant, prosthesis

Implantable photonic probes are of increasing interest to the field of biophotonics and in particular, optogenetic neural stimulation. Active probes with onboard light emissive elements allow for electronic multiplexing and can be manufactured through existing microelectronics methods. However, as the optogenetics field moves towards clinical practice, an important question arises as to whether such probes will cause excessive thermal heating of the surrounding tissue. Light emitting diodes typically produce more heat than light. The resultant temperature rise of the probe surface therefore needs to be maintained under the regulatory limit of 2°C. This work combines optical and thermal modelling which have been experimental verified. Analysis has been performed on the effect of probe/emitter geometries, emitter, and radiance requirements. Finally, the effective illumination volume has been calculated within thermal limits for different probe emitter types and required thresholds.



hyperpolarising (inhibiting) chloride ions into the nerve cell, thus reducing or preventing nerve cell activity. These techniques have been demonstrated in many neuroscience studies, e.g. by Busskamp et. al. (3). Perhaps more significantly to the biomedical engineering community, the technique is now moving towards clinical practice, with interest in retinal prosthesis (e.g. (4, 5)), visual brain prosthesis, and brain pacemaking activity for conditions such as epilepsy. At the time of writing, there are trials underway for optogenetic retinal prosthesis, and various groups are starting the process of developing clinically approved devices for more invasive brain prostheses for conditions such as epilepsy.

1. Introduction

Optogenetics is a gene therapy technique to incorporate light-sensitive proteins into cells. The field began with demonstration of channelrhodopsin-2 (ChR2) proteins ectopically expressed in frog oocytes in 2003 (1). ChR2 is a light-sensitive cation channel and therefore allows optical depolarisation (stimulation) of nerve cells. Complementary to light-sensitive ion channels are light sensitive pumps such as the chloride pump - halorhodopsin (NpHR) (2). NpHR acts to pump

This article has been accepted for publication and undergone full peer review but has not been through the copyediting, typesetting, pagination and proofreading process, which may lead to differences between this version and the [Version of Record](#). Please cite this article as [doi: 10.1002/jbio.201700358](https://doi.org/10.1002/jbio.201700358)

For typical laboratory experiments, light delivery can be achieved via laser coupled optical fibres. Being external, power consumption and thermal dissipation is not an issue to such devices if the intensities are kept to moderate levels above the stimulus threshold. In contrast, technology for chronic long-term implants in freely moving animals or medical neuroprostheses are still relatively immature. Two primary sources of ‘optrodes’ - the optical equivalent of the electrode - have been explored: Waveguiding (6, 7) and local photogeneration (8, 9). The former generates light far from the tissue and then delivers it to the target via a delivery system with multiple light guides. The latter aims to generate light on the implantable structure.

The key caveat of optogenetics from the perspective of light delivery systems is that the illumination required to stimulate neural tissue is very high. Cultured cells encoded with wild-type ChR2 typically require photon fluxes of $10^{17} - 10^{19}$ photons $s^{-1} cm^{-2}$ ($0.4 - 40 mW/mm^2$) to achieve a full dynamic range of photocurrent response ((10-12)). Classically, reliable neural firing at 20Hz has required $0.7 mW/mm^2$ (11). There has also been some evidence that in-vivo, the requirement is somewhat less. For example, Bi et al. (4) noted an S-curve dynamic range of photocurrent with the logarithm of irradiance between $10^{16} - 10^{19}$ photons $s^{-1} cm^{-2}$ ($40 \mu W/mm^2 - 40 mW/mm^2$) in retinal ganglion cells. Lagali et al (13) noted a range of $10^{14} - 10^{17}$ photons $s^{-1} cm^{-2}$ ($4-400 \mu W/mm^2$) in retinal bipolar cells.

The resultant emission requirement can put a strain on the probe photonics. Thus, there has been a considerable effort in exploring the biophysics of ChR2 (10, 12) and developing more efficient variants. One example is the CatCh (11) variant of ChR2, which utilizes a Ca^{2+} feedback mechanism to bring sensitivity down to $10^{16}-10^{17}$ photons $s^{-1} cm^{-2}$. Another example is melanopsin which is connected to a G-protein cascade giving amplification and resulting in a sensitivity of 10^{12} photons $s^{-1} cm^{-2}$ (14). Neither of these is ideal – The Ca^{2+} permeability of CatCh may interfere with cell metabolism and the response time of melanopsin is very long (~10s). However, they demonstrate that we can expect to see a range of required thresholds in the future depending on the opsin used and the target tissue type.

Probes with light emissive elements have an advantage over light guided systems in that they can perform onboard multiplexing. In particular, probes with in-built control circuits (15, 16) hold the potential for large-scale multi-emissive systems. However, from an engineering perspective, no light emitter is 100% efficient. In fact, typical efficiencies range from about 5% (9, 17, 18) for micro-light emitting diodes (μ LEDs) to 80% (19) for best in class LEDs. There is, therefore, a danger that such probes will form surface hot spots that exceed the $2^\circ C$ regulatory limit if driven too hard. An alternative perspective of the same issue is that for the given thermal limit, their radiance may not achieve sufficient stimulation at significant penetration depths.

The key question, therefore, arises as to how far light can penetrate into tissues for a given thermal limit. McAlinden et al. (9) discussed the optical and thermal characterization of their respective monolithic gallium nitride optrode. Similarly, Wu et al. (18) demonstrated and characterized a silicon probe with integrated micro-light emissive elements. However, a comprehensive analysis of thermal effects for different substrate configurations and dimensions, and opsin sensitivities has not yet been performed.

In this work, we combine an optical scattering model of light propagation in tissue (20, 21) with a finite element model of tissue heating effects. We calibrate these with experimental data from real probes and then simulate a concept probe to explore key questions in the field:

- (1) What are the light penetration depth and volume for a given emission power and different LED geometries and emission profiles?
- (2) What is the maximum energy dissipation that may be allowed while keeping surface hotspots within acceptable limits?
- (3) Given the two parameters above, what volume of tissue can be illuminated for different levels of gliosis around long-term implants?

We hope this work can provide the basis for future optrode designs based on active light emissive modules.

2. Methodology

Our objective is to use optical and thermal modelling to explore the interplay between illumination and thermal profiles for different emitter geometries and probe architectures. In particular, we aim to determine the maximum optical penetration depth and volume for a given thermal limit. To achieve this, we model the effect of light scattering in tissue with a 4-state biophysical model of the photoresponse of the channelrhodopsin.

2.1 Tissue thermal limit

In 1989 Lamanna et al. (22) performed acute experiments on anaesthetized rats and suggested that temperature should not increase more than $1^\circ C$ above ambient. This threshold has since been used in over 60 other studies (e.g. (9, 23)). However, the $1^\circ C$ limit refers to the threshold where the authors started to see abnormal signalling. They did not observe actual tissue damage while transient increases were kept below $5^\circ C$. Similarly, Matsumi et al. (24), and Fuji et al. (25) respectively inserted heated probes into non-human primate brains and independently determined the thermal limit of $43^\circ C$, i.e. $\Delta T = 6^\circ C$. More recently in 2012 Opie et al. (26) looked at ex-vivo tissue and determined

38.7°C as the threshold at which damage becomes apparent in the retina. But, perhaps the retina is less prone to thermal damage than brain tissue due to its various mechanisms to protect itself from phototoxicity. Goldstein et al. (27) observed cell death in neuronal cells of the central nervous system after 60 minutes at temperatures as low as 40.5°C.

The specific condition of these studies is that they are acute, with sacrifice and histology a few days after the experiment. There are very few chronic long-term studies of the effect of raised temperatures. Seese et al. (28) and Okazaki et al. (29) demonstrated that $\Delta T = +2^\circ\text{C}$ is tolerated in muscle. However, the long-term effects in the up-regulation of heat shock proteins, and glial response in the central nervous system has not been published. This is a challenge that needs to be explored in more detail by the biology community.

It is therefore perhaps not surprising that the regulatory guidance is also limited. Directive 93/42/EEC simply states: “*Devices must be designed and manufactured in such a way as to remove or minimise as far as is possible: <temperature rise>*”. The American Association of Medical Instrumentation (AAMI) recommend a limit of $\Delta T = +2^\circ\text{C}$, which seems in keeping with the review above, i.e. $T \leq 39^\circ\text{C}$.

We, therefore, suggest 2 limits: (i) for basic experimental neurobiology, the evidence suggests that a 1°C limit would prevent thermally induced activity. (ii) For translational efforts, the regulatory limit is 2°C for any surface hotspot.

2.2 Thermal transmission modelling

The flow of heat through different media can be represented by a series of linear equations which can be solved using finite element analysis. Assuming the whole optrode is floating in the tissue solution, the temperature rise of the optrode can be predicted by solving the time-resolved heat equation:

$$\rho C \frac{\partial T}{\partial t} = \nabla \cdot (k \nabla T) + Q_0 \quad (1)$$

Where T is the temperature, t is the time, ρ is the medium density, C_p is the specific heat capacity, k is the thermal conductivity (assumed to be a constant across a single medium), and Q_0 is the heat source.

There are a number of potential heat sources in an optrode. If it contains active electronic components, then these can dissipate heat wherever there is significant power consumption. However, for this work, we consider the μLED as the primary heat source with defined thermal emissions for given time periods and repetition rates. This is because its power consumption is in the milliwatt range, whereas implantable circuitry typically has significantly lower power consumption.

We consider the μLED as an even surface heat source so $Q_0 = Q$. The Neumann boundary condition can then be applied to the surface heat source:

$$-n \cdot (-k \nabla T) = Q_0 \quad (2)$$

Where n is the normal directional vector to the surface of the emitter. Working with such models, in 2007, Kim et al. (23) demonstrated modelling of thermal dissipation through Utah arrays (8 x 8 array of penetrating silicon probes) in both phantom media and cat cortex. They found that 13mW of power dissipation ($=81 \mu\text{W}/\text{mm}^2$) resulted in a temperature rise of 0.43°C . McAlinden et al. (9) also explored the thermal dissipation relative to optical output for an all-gallium nitride-based optrode. Their model produced a temperature rise of 1°C over 10ms at an output radiance of $600 \text{ mW}/\text{mm}^2$ and a final (saturated) temperature rise of 1.5°C .

There are, however, some further complications. The first is that in addition to passive flow, there is also an active heatsinking effect from vasculature in the cortical tissue. This removes thermal energy at a higher rate than would otherwise be expected. For example, Kim et al. (23) found the temperature rise to be 22% lower in cortical tissue than in a passive phantom construct. Opie et al. (26) found the temperature rise to be up to 6 times lower.

The second complication is that it was recently shown by Stujenske (30) that light absorbed by the tissue could raise its temperature. We thus modify the Pennes' model (31) of bio-heat transfer to include the optical absorption effect:

$$\rho C \frac{\partial T}{\partial t} = \nabla \cdot (k \nabla T) + \rho_b C_b w_b (T - T_b) + Q_m + Q_a(x, y, z, t) \quad (3)$$

Where the second, third and fourth term on the right of the equation denotes heat dissipated through the blood vessels, metabolic heat (Q_m) and heat generated from light absorption (Q_a), respectively. P_b , C_b , w_b and T_b denote the density, heat capacity, average perfusion velocity and temperature of the blood in the vessels, respectively. To solve (3), we utilize COMSOL Multiphysics (V5 with the (bio)heat transfer module) to perform the thermal analysis.

We developed two probe models shown in Figure 1 (a,b). (a) is a model of a custom-made probe we have developed to calibrate the simulations. (b) is a model of a general purpose multi-LED concept probe which we would foresee being utilised in clinical practice.

We envisage the concept probe either as a solitary device or as part of an array, typically having a spacing of around 1 mm. The probe head would need a height of 2 mm or less to fit in the skull. As such, we chose exemplar head dimensions of $1 \times 2 \text{ mm}$. Such an area is sufficient to accommodate multiplexing electronics, amplifiers and digital to analog conversion (15, 16). The shaft would typically have both LEDs and recording electrodes. An exemplar of a comparable recording-only

probe is the *Neuropixels probe* (32). As the human cortex is between 2 mm and 3.5 mm in length (33), we determine the length of this probe to be 5.5mm to allow for gliosis effects pushing the probe up slightly from the cortex and the thickness of any mechanical baseplate.

For simplicity, we consider 8 LEDs and recording sites for this probe to interact with each of the 6 cortical layers with some redundancy. It should be noted that for comparison, some high-density probes, e.g. by Lopez et al. (34), and Angotzi et al. (35) have hundreds of recording sites. We also simulate each probe as an individual entity. It may well be that probes are arranged in a 4x4 or 8x8 penetrating matrix. In such a scenario, there would be a larger surface area from which to dissipate heat, and possibilities of heat transfer between probes. However, we feel this would complicate the analysis. Furthermore, from our simulations, the most important hotspots are local to the area around individual LEDs, and the probe shaft. Thus, we focus on the individual optrode configuration shown in Figure 1(b).

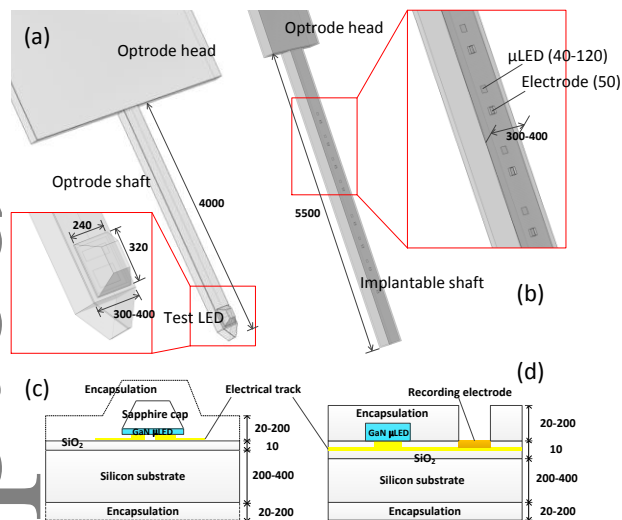


Figure 1 The COMSOL models of the calibration test probe (a) and the exemplar probe (b). The layers profiles for each are given in (c) and (d) respectively. Typically, the core of such probes is made of silicon. Electrical lines are aluminium, electrodes are gold, and passivation is SiO₂. The LED is made of gallium nitride, and there is an additional silicone encapsulation on top.

The dimensions of the exemplar probe, plus a custom test probe used in the experimental validation are given in Table 1. Where dimensions are defined as a constant, we have used a specific value. Where dimensions are defined as a variable, we have explored the effect of different dimensions on the thermal outcome. In these simulations, we use the same value for width and thickness, which means that the optrode shaft has a square shape. It should be noted that this may be different for future probes which may be thinner with respect to their width. We only simulate down to thicknesses of 100μm. However, for even thinner probes,

we would expect the greater surface area to bulk ratio to support higher dissipation for long-term heat transfer. Simultaneously, for short pulses, a reduced bulk would have a reduced capacity to temporarily store (smooth) spikes in heat generation.

Table 1: Probe dimensions for the thermal modelling.

Optrode element	Dimension (μm)		Type
	Test probe	Exemplar	
Head width	3000	1000	Const
Head length	4000	2000	Const
Head substrate thickness	200	100 - 400	Var
Shaft length	4000	5500	Const
Shaft width	400	100-400	Var
Shaft substrate thickness	200	100-400	Var
Emitter diameter	240x320	20-120	Var
Electrode diameter	50	50	Const

The layer structure of the optrode is given in Figure 1(c). We assume that active emitting optrodes will have a silicon core with metal control lines and emitter (typically a gallium nitride μLED). The metal control lines are typically coated with a silicon dioxide dielectric. For CMOS (complementary metal oxide semiconductor) devices, there would also be a thin silicon oxy-nitride top layer. But as it is thin, and its thermal conductivity is much higher than silicon dioxide or the polymer encapsulation layer, its effect will be negligible compared to its neighbouring layers. We thus ignore this layer.

The whole structure will be coated with a polymer encapsulant which acts as a biocompatible interface. Poly-dimethylsiloxanes (PDMS/silicone) and parylene-C, epoxies and urethanes are typical choices for encapsulation. These are chemically different and vary considerably in glass transition temperature. But for the operational range of these devices, their thermal properties are very similar. We have thus used representative values, for “polymer” in Table 3. For the test probe, we used PDMS as the primary encapsulant.

The dimensions of the individual layers simulated are given in Table 2.

Table 2: Probe layer thicknesses for the thermal modelling.

Optrode element	Thickness (μm)	Type
Polymer encapsulation	10 – 100	Variable
Silicon core	100-300	Variable
GaN μLED	1-100	Variable

Al driving track	1	Constant
SiO ₂ passivation	5	Constant
Au electrode	1	Constant

The material parameters of the constituent layers used in the thermal analyses are shown in Table 3.

Table 3: Simulation parameters for the thermal modelling.

Medium	k, W/(m·K)	ρ , kg/m ³	Cp, J/(kg·K)
Tissue	0.6	1057	3600
GaN	200	6150	485
Sapphire	42	400	854.8
SiO ₂	1.5	2500	966
Silicon	149	2329	706.75
Gold	315	1930	129
Polymer	0.15	965	1460

For optogenetics, short optical pulses (<100 ms) are generally used rather than continuous illumination. So, the primary concern is the transient temperature change from the device. Q_0 (the heat source) is determined by the inefficiencies in the optical generation by the LED. This can be given by:

$$Q_0 = (1 - \eta_{LED}) \cdot V_{LED} I_{LED} \quad (4)$$

Where η_{LED} is the efficiency of the LED which denotes the ratio between optical power output and electrical power input; V_{LED} and I_{LED} are the bias voltage and bias current, respectively.

A fixed 37°C is used as the boundary condition, ignoring metabolic heat generation. For the test probe described in Figure 1 9a), we used mini LEDs with an efficiency of around 30% (36), i.e. 70% of the applied electrical energy would convert to heat.

We set continuous boundary conditions for inner boundaries, while for outer boundaries we set a heat convection boundary condition (equation (5)):

$$-n \cdot (-k\nabla T) = h \cdot (T_{ext} - T) \quad (5)$$

Where T_{ext} is the temperature usually being constant for the external environment and h is the heat transfer coefficient of the boundary material. For the tissue boundary in the model, we set h at 1000 W/(m²·K) as this would be a typical value (37).

2.3 Optical systems

Opsin absorption can be tuned from the near ultraviolet across to the red region of the visual spectrum. Peak absorption varies between 470 – 590nm. A full review of the wavelength selectivity of different opsins can be found in the review by Kurihara and Sudo (38). In this range, micro-lasers are still relatively immature, so

we primarily focus on LEDs. In particular, we consider gallium nitride (typical peak ~470nm) – the primary technology used in modern high radiance lighting.

The illumination penetration profile into tissue is largely dependent on the total amount of light being emitted. As light is generated by electron-hole recombination, this means higher drive current. Smaller LEDs will, therefore, require higher drive current densities to achieve the same emission profile. However, this means that they are more susceptible to “droop”. Droop is a phenomenon well documented within the LED community whereby the efficiency has an inverse relationship with the current density. It was recently attributed to Auger recombination by Iveland et al. (39).

Figure 2(a) combines data from our previously presented μ LEDs (17) with the efficiency profile of commercial mini-LEDs (Cree Corp DA2432 (36)). The latter is both (currently) the smallest commercially available LED and the largest (size: 320 × 240 μ m, emission surface 280 × 210 μ m) conceivable LED that could be placed on an optrode. We also include the profile taken from the best efficiency we have seen in the published literature (Narukawa et al. (19)).

The micro-LED efficiency (3-5%) is comparable to that presented by McAlinden et al. (3-5%) (9) but significantly higher than that presented by Wu et al. (18) (0.8%). It should be noted that none of these studies used integrating spheres for their measuring technique. So, the efficiency may be an underestimation. From the micro/mini LEDs, we created a model for the full range of current densities on the basis of a curve fit. The output of this model for different LED sizes and input powers can be seen in Figure 2(b).

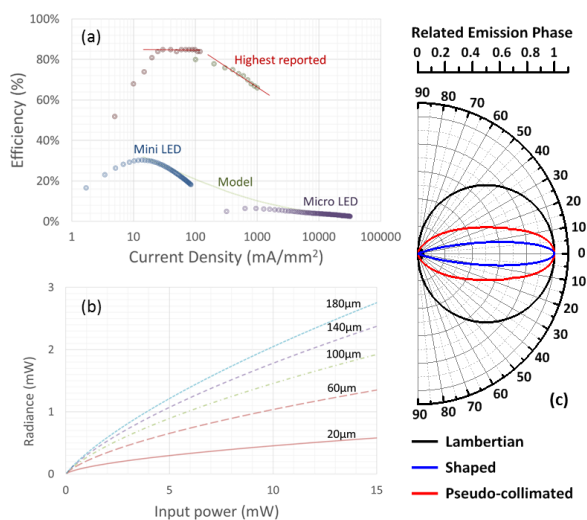


Figure 2 Electro-optical conversion efficiency of LEDs (a) Measured efficiencies from mini LEDs, micro LEDs and an empirical model of what is currently available. Also plotted is the highest reported LEDs in the literature. (b) Assuming the model in (a), the radiance vs input power profile for different

LED sizes. (c) The emission profile of the three types of LEDs (see 2.3).

LEDs, however, cannot be used in isolation. There is a small overhead due to the transistor driving electronics. i.e. the drive transistors typically require a combined source-drain voltage drop of 0.5V to 1V, compared to 2.5V-3.5V for the operation of the LED. If there are significant contact and/or line resistances, these will take additional voltage drops. As such, we assume LED system efficiencies (i.e. including the driving transistors) to be around 75% of the LED only efficiency. If the driving electronics are elsewhere, this perhaps is only interesting to the battery life. However, if the driving circuitry is also incorporated into the silicon of the optrode – i.e. an active optrode, then it needs to be included.

2.4 Emitter emission profile

The emission profile – i.e. how the light spreads from the LED upon emission is an important determinant in the light penetration profile. We consider 3 types of emission profile, as shown in figure 2(c).

Lambertian: The standard emission profile for LEDs without surface texturing (36). The phase is theoretically proportional to the cosine of the deflection angle.

Shaped: Includes rear beam shaping optics which tighten the emission profile such as demonstrated in (40).

Pseudo-collimated: Conceptual LEDs which include with both rear beamshaping and frontal micro-lens optics, e.g. in (41)

Although the DA2432 mini-LED is rectangular, there is some evidence from the literature that for micro-LEDs a circular shape is more efficient (40). Thus, for our simulations, we assume this configuration.

2.5 Optical modelling

As the tissue is usually seen as a highly-scattering medium, the spatial irradiance distribution from the optrode light emitters into the tissue can be phenomenologically analysed with a Monte Carlo photon transportation model (42). Hereby, the macroscopic light diffusion in the tissue can be obtained through the statistical behaviours of numerous photons traversing the tissue. The irradiance distribution can then be expressed through the integral of the photon probability fluence.

Incident phase

The simulations begin with a circular μ LED of a given profile and diameter in tissue. An incident phase profile is setup with a random initial position for the photons. The initial directions of the photons are determined by the emission profile of the emitter as described in 2.4.

Photon transportation in the tissue

The photon transportation and the scattering events in the tissue are controlled by the inherent optical properties of the tissue. The properties here are the scattering coefficient μ_s , the absorption coefficient μ_a and the asymmetry factor g (43). The mean free path l of the photon between two scattering sites is controlled by the scattering and absorption coefficients and a pseudo-random number ξ (42):

$$l = -\ln \xi / (\mu_s + \mu_a) \quad (6)$$

Where $\mu_s + \mu_a$ is defined as the extinction coefficient μ_e . Once a local particle scatters the photon it changes the direction in probability distribution obeying the phase function $p(\theta)$, which has a strong connection to the asymmetry factor g :

$$g = \frac{1}{4\pi} \int p(\theta) \cos\theta \cdot d\omega \quad (7)$$

Where θ is the scattering angle. It also loses a fraction of the intensity weight which is the proportion of μ_a/μ_s to the total current weight. The lost fraction is added to the local grid to update the photon deposition matrix for the calculation window; then the photon moves along a new direction determined by the scattering phase with the updated weight until the weight decreases below a reasonable extinction threshold.

Therefore, the light diffusion profile in the tissue for the emitter can be obtained from the statistic of numerous photon behaviours.

Combined scattering

The scattering mismatch in the brain tissue results from a heterogeneous arrangement of cellular and sub-cellular structures of various shapes and sizes. For simplicity we assume the various scattering structures to be spherical particles of different sizes floating in the host medium. The total scattering results from a mixture of Mie scattering and Rayleigh scattering (20).

We assume the refractive index of the host medium and the scattering particles are n_e and n_p respectively. We assume n_p to be complex, $n_p = n_p' + in_p''$, and n_e to be real. We use ρ_p and λ to denote the volume density of the scattering particles, and the operating wavelength in the vacuum, respectively. The main refractive index contrast $m = n_p/n_e$.

We also use d_p as the diameter of the scattering particle, but it is diverse for Mie and Rayleigh scattering. We can define the size contrast α in the brain tissue as:

$$\alpha = \pi n_e d_p / \lambda \quad (8)$$

$\alpha \ll 1$ for Rayleigh scattering and $\alpha \sim 1$ for Mie scattering. As the size distribution in the brain tissue is complicated, for simplicity, we assume $d_p = d_{Mie}$ for Mie scattering and $d_p = d_{Rayleigh}$ for Rayleigh scattering where d_{Mie} and $d_{Rayleigh}$ are the average diameters for Mie and Rayleigh particles respectively.

We assume $0 \leq f_{Mie} \leq 1$ is the fraction of Mie scattering so that $0 \leq f_{Rayleigh} \leq 1$ is the fraction of Rayleigh scattering and the fractions satisfy: $f_{Mie} + f_{Rayleigh} = 1$ (20).

Thus, the scattering and absorption coefficients are weighted summations of Mie and Rayleigh coefficients:

$$\mu_s = f_{Mie} \cdot \mu_s^{(Mie)} + f_{Rayleigh} \cdot \mu_s^{(Rayleigh)} \quad (9)$$

$$\mu_a = f_{Mie} \cdot \mu_a^{(Mie)} + f_{Rayleigh} \cdot \mu_a^{(Rayleigh)} \quad (10)$$

The total phase function of the tissue is also the combination of Mie and Rayleigh scattering:

$$p(\theta) = f_{Mie} \cdot p_{Mie}(\theta) + f_{Rayleigh} \cdot P_{Rayleigh}(\theta) \quad (11)$$

Mie and Rayleigh scattering

The Mie scattering coefficient can be derived from the Mie-Lorentz theory (21):

$$\mu_s^{(Mie)} = \frac{\rho_a \lambda^2}{2\pi} \sum_{n=1}^{\infty} (2n+1) (|a_n(m, \alpha_{Mie})|^2 + |b_n(m, \alpha_{Mie})|^2) \quad (12)$$

Where a_n and b_n are the Mie coefficients, and in practice, we usually use $n_{max} = \alpha + 4\alpha^{1/3} + 2$ as the maximum limit of the summation. As defined before, m is the main refractive index contrast and $\alpha_{Mie} = \pi n_e d_{Mie} / \lambda$ is the main size contrast in the Mie scattering.

For Rayleigh scattering, we have $\alpha_{Rayleigh} = \pi n_e d_{Rayleigh} / \lambda \ll 1$, where $d_{Rayleigh}$ is the diameter of the Rayleigh particle. So, the Rayleigh cross section can be calculated by the following equation:

$$\begin{aligned} \mu_s^{(Rayleigh)} &= \frac{2\pi^5 d_{Rayleigh}^6}{3 \lambda^4} \left(\frac{n_p^2 - 1}{n_p^2 + 2} \right)^2 \quad (13) \\ &\ll \frac{2\pi}{3} \left(\frac{n_p^2 - 1}{n_p^2 + 2} \right)^2 \frac{\lambda^2}{n_e^2 \pi^2} \end{aligned}$$

The Rayleigh scattering coefficient is usually 2-3 orders of magnitude lower than the Mie scattering coefficient in tissue. The Mie extinction coefficient can then be calculated using Mie-Lorentz theory (21):

$$\mu_e^{(Mie)} = \frac{\rho_a \lambda^2}{2\pi} \sum_{n=1}^{\infty} (2n+1) \text{Re}(a_n(m, \alpha) + b_n(m, \alpha)) \quad (14)$$

Thus, we have $\mu_a^{(Mie)} = \mu_e^{(Mie)} - \mu_s^{(Mie)}$. Assuming the absorption cross-section is proportional to the area of the

particle cross-section, we have: $\mu_a^{(Mie)} / \mu_a^{(Rayleigh)} = (d_{Mie} / d_{Rayleigh})^2$. So, we obtain the total absorption coefficient μ_a :

$$\mu_a = \mu_a^{(Mie)} \cdot (f_{Mie} + f_{Rayleigh} \cdot \left(\frac{d_{Rayleigh}}{d_{Mie}} \right)^2) \quad (15)$$

The Mie phase function $p_{Mie}(\theta)$ can be obtained in the Mie-Lorentz scattering theory (21):

$$p_{Mie}(\theta) = \frac{|S_1(\theta)|^2 + |S_2(\theta)|^2}{4\pi \cdot \sum_{n=1}^{\infty} (2n+1) (|a_n|^2 + |b_n|^2)} \quad (16)$$

Where $S_1(\theta)$ and $S_2(\theta)$ are the scattering amplitudes of a certain scattering angle θ . More details of the derivation of these intermediate parameters with the involvement of spherical Bessel functions can be found in the paper by Bohren et al.(21). The Rayleigh phase function $p_{Rayleigh}(\theta)$ is proportional to $1 + \cos^2\theta$.

Parameters

Table 4 gives the main simulation parameters in the optical analysis. Among these parameters the operating wavelength λ is usually determined by the opsin we use, typically 470nm for ChR2.

Table 4: Simulation parameters used in the optical analysis

Parameter	Value	Description
λ	0.47 μ m	Operating wavelength
n_e	1.36	Refractive index of the host medium (44)
n_p	1.48+0.001j	Refractive index of the scatter particle (45)
$n_{polymer}$	1.59	Refractive index of the polymer (46, 47)
$n_{sapphire}$	1.76	Refractive index of the sapphire (48)
n_{GaN}	2.43	Refractive index of the GaN (49)
d_{Mie}	0.6 μ m	Mie particle mean diameter (50)
$d_{Rayleigh}$	0.01 μ m	Rayleigh particle mean diameter. derived from: $\alpha \ll 1$ in Rayleigh scattering
ρ_p	1.3×10^{-10} mol/L	Particle volume density (51)
f_{Mie}	0.8	Mie scattering fraction. Derived from (20)
$f_{Rayleigh}$	0.2	Rayleigh scattering fraction. Derived from (20)

The main refractive index contrast of the brain tissue can be the difference between the cytoplasmic solvent and unsolvable lipid particles (44). Drezek et al. have reported that the refractive index of tissue varies from 1.36 of the extracellular fluid to 1.7 (44). The measured refractive index of the scattering particles in human tissue is from 1.4 to 1.48 for visible light (45). So, we set n_e and n_p to 1.36 and 1.48 respectively.

The Mie particle diameter d_{Mie} should vary from 0.1 to 1 μm (50). For Rayleigh particle the size contrast $\alpha \ll 1$, so we assume $d_{Rayleigh} = 0.01 \mu\text{m}$.

The experimentally measured optical properties of the brain tissue including μ_s , μ_a , μ_e and g are reported by Yaroslavsky et al.(43) and Taddeucci et al.(51) before. In the grey matter, for the typical operating wavelength, the measured scattering coefficient μ_s varies from 7.8 to 12.5 mm^{-1} ; the measured asymmetry factor g varies from 0.87 to 0.9. The absorption coefficient μ_a is 2~3 orders of magnitude smaller than μ_s so light diffusion profile in the tissue is not sensitive to μ_a . The particle volume density ρ_p should be between $1 \sim 10 \times 10^{-10}$ M. Given these statements we estimated the input parameters.

The scattering-absorption ratio μ_a/μ_s is no more than 0.01, so we assume this to be 0.01 around the responding peak of the opsins. Thus, the imaginary part of the refractive index n_p'' can be derived. The specific ρ_p , f_{Mie} and $f_{Rayleigh}$ are also derived from experimentally reported values for the tissue.

2.6 Tissue deadzone

Reactive gliosis is a common pathological feature which commonly encapsulates surgical implants in neural tissue, for example, deep brain stimulators (52). Specifically, a thin capsule of glial cells containing inflammatory cells such as macrophages and lymphocytes forms around the device (52). Szarowski et al. demonstrated that when neural prosthetic devices were implanted in rats, glial encapsulation has been shown to extend up to 100 μm around the device, 12 weeks post-insertion (53). Similar patterns of long-term gliosis have also been reported in non-human primates, 3 years post-implantation of electrodes (54).

The issue with such gliosis regions is that any neurons contained within are effectively dead or inactive, and therefore no longer contributes to the surrounding neural circuitry. As such any stimulus to be effective must be effective beyond this region.

Such effects are not seen in acute experiments. So for example, although Wu et al. (18) demonstrated light penetration of only 50 μm (beyond the ChR2 threshold), they could still see strong neural responses. However, for chronic long-term implants, this needs to be considered. For example, if the light penetration above the ChR2 threshold was only 100 μm , and the gliosis thickness was 100 μm , no net stimulus could be expected.

So, to calculate the volume of stimulus, we define the glial region as the “dead zone”, i.e. no effect from the light. We then look at an optimistic case (100 μm), and pessimistic case (200 μm) for dead zone thickness.

3. Experimental Validation

3.1 Optothermal measurement of optrodes

We developed a test optrode according to the dimensions in Table 1. It consists of a simple silicon shaft and head. At its tip is a single CREE DA2432 mini LED (36). Titanium-gold lines connect the LED to the wire-bonded connectors in the head. For experimentation, the optrode was placed on a PCB ceramic base.

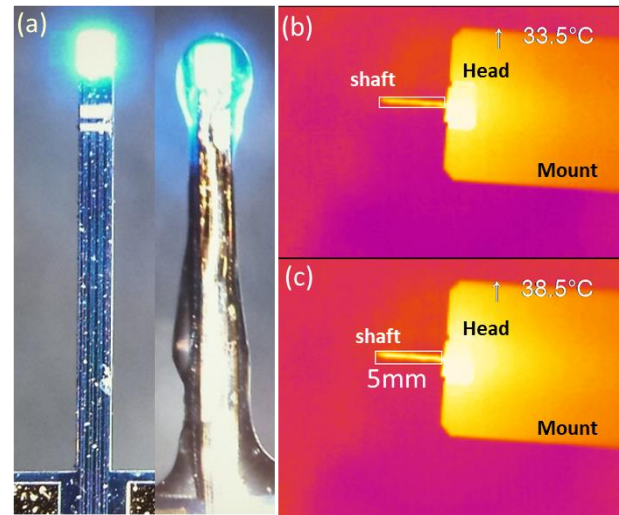


Figure 3 LED emission Top-view Photograph of the optothermal measurement experiment. (a) 2 LEDs turned on under visible camera; (b) single LED turned on under IR camera; (c) 4 LEDs turned on under IR camera.

The LED on the optrode was operated with large current ranges from 10mA to 25mA. This is around 20 times the range we would expect in practice (i.e. 0.5-1.5mA). However, such a large range allows for accurate measurement with our experimental equipment. Measurements of the optrode surface temperature in air were taken with an Optris microbolometer thermal camera. The measurements were taken in an enclosed space with the baseline air temperature measured at a constant 28°C. Both continuous wave (up to 15 minutes) and pulses were tested to show a broad range of the thermal effect on the optrode.

The optrode devices can be seen in Figure 3 (a) shows LED emission from a bare LED optrode (left) and an encapsulated optrode (right). Figure 3 (b,c) shows the optrode from the perspective of a thermal camera at two different temperatures. The apparently warmer head part of the optrode is a reflectance artefact. The actual temperature at the tip could be determined by the change in temperature of the specific pixels with LED activity.

3.2 light penetration measurement of tissue

To ensure the validity of the optical modelling we performed experiments to compare with the modelling results. We, therefore, created an experiment with a light

guided cannula which was inserted laterally, but near the surface of brain tissue. The transmission profile could be monitored via the microscope imaging system.

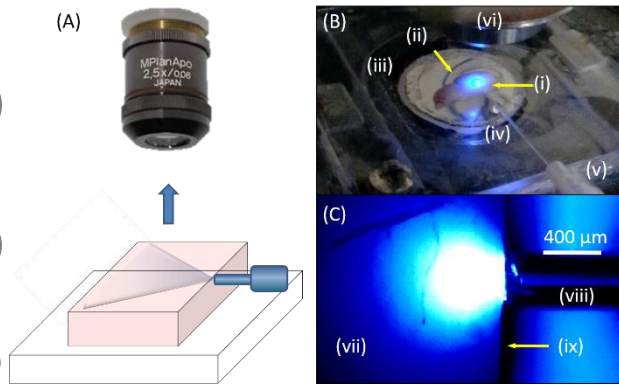


Figure 4 Experiment results show the light penetration properties of the tissue. (A, B) Diagram and photograph of the experimental setup. (C) Top view of the fibre optic touching the side of the brain. (i) Right hemisphere of a mouse brain (sagittal cut), (ii) dorsal surface of the brain from where the light transmission is measured (surface horizontally cut), (iii) chamber filled with ACSF to keep the brain fully submerged, (iv) ceramic cannula, (v) fibre optic, (vi) microscope objective, (vii) dorsal surface of the brain from where the light transmission is measured (surface horizontally cut), (viii) ceramic cannula, (ix) right hemisphere of a mouse brain (sagittal cut). Light was delivered on the lateral internal side (sagittal plane) of the brain.

To achieve this, brains were extracted from 6-week old C57BL6 mice to represent typical brain tissue. The brain was quickly removed after cervical dislocation and dissected in two hemispheres along the sagittal line. Each hemisphere was subsequently cut along the dorsal surface forming a 90-degree angle between the dorsal and sagittal planes. The brain hemisphere was then placed in a microscope (Olympus BX 61, upright) stage chamber submerged in ACSF (Figure 4 (B)) at room temperature with the dorsal surface (ii) facing upwards for observation through the microscope lens (Olympus 2.5X NA, (vi)). The sagittal plane (ix) was placed facing a 400µm diameter cannula tip (viii) connected to a LED via a fibre optic (v).

Light stimulation was performed using CoolLEDs precise Excite LEDs (470 nm, 585 nm). Light penetration measurements were taken with an Andor iXon DV887 back-illuminated EMCCD camera and the images of the brain dorsal surface acquired with Andor Solis software. The LEDs normalized light intensity was set immediately under the maximum brightness level the Andor camera could accept (14 bits) and the brightness intensity curve measured on the X and Y planes (X plane correspond to the coronal brain section; Y plane correspond to the sagittal one).

4. Results and discussion

4.1 Thermal modelling results

To demonstrate the validity of the thermal modelling analysis, we performed a comparison of experimental results from the optrode shown Figure 3 and its COMSOL model described in Figure 1 (a) and Table 1. Both experiment and model were in air and results have been presented in Figure 5.

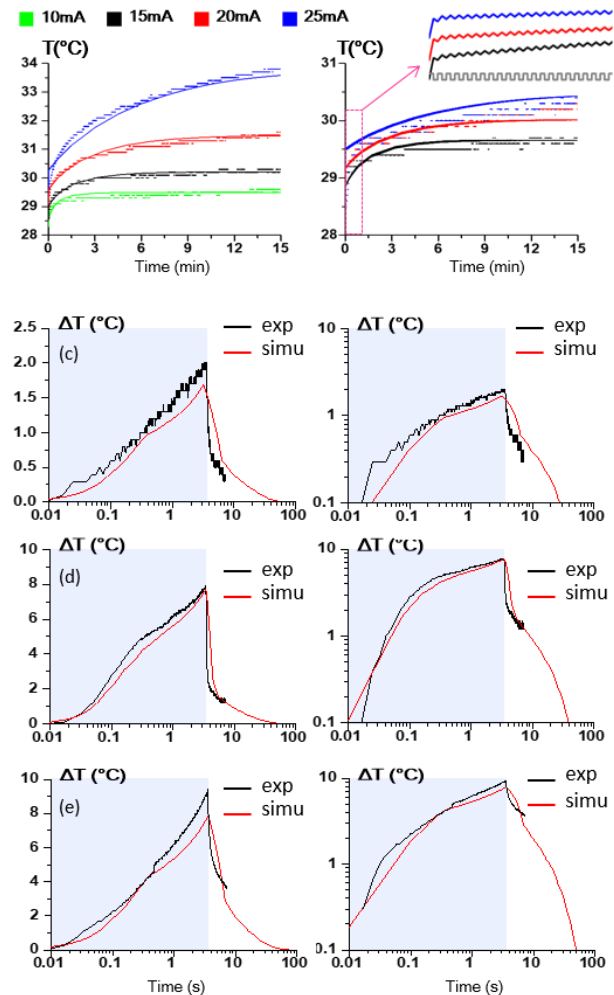


Figure 5 Temperature change results show coincidence of the thermal modelling to the experiment results: (a) 15min CW stimuli; (b) 15min pulsed stimuli. (c) 3.5s single pulsed stimulus of 2.44mA; (d) 3.5s single pulsed stimulus of 7.1mA; (e) 3.5s single pulsed stimulus of 8mA.

Figure 5(a) and (b) show the effect of long-term heating over 15 minutes for both (a) continuous wave (CW) LED illumination and (b) pulsed stimuli situation respectively. In the pulsed stimuli situation, the temporal profile of the pulsed stimuli is pulse series with the pulse width of 0.7s and the duty ratio of 50%, temperature in the first minute is zoomed in to see the oscillation of the

temperature change along the pulsed stimuli. The quantization error that can be seen is due to the 0.1°C accuracy of the thermal camera.

Figure 5(c – e) shows the effect of heating from short 3.5 second pulses from a CREE LED optrode in air. The shaded regions define the 3.5 s period with the LED on,

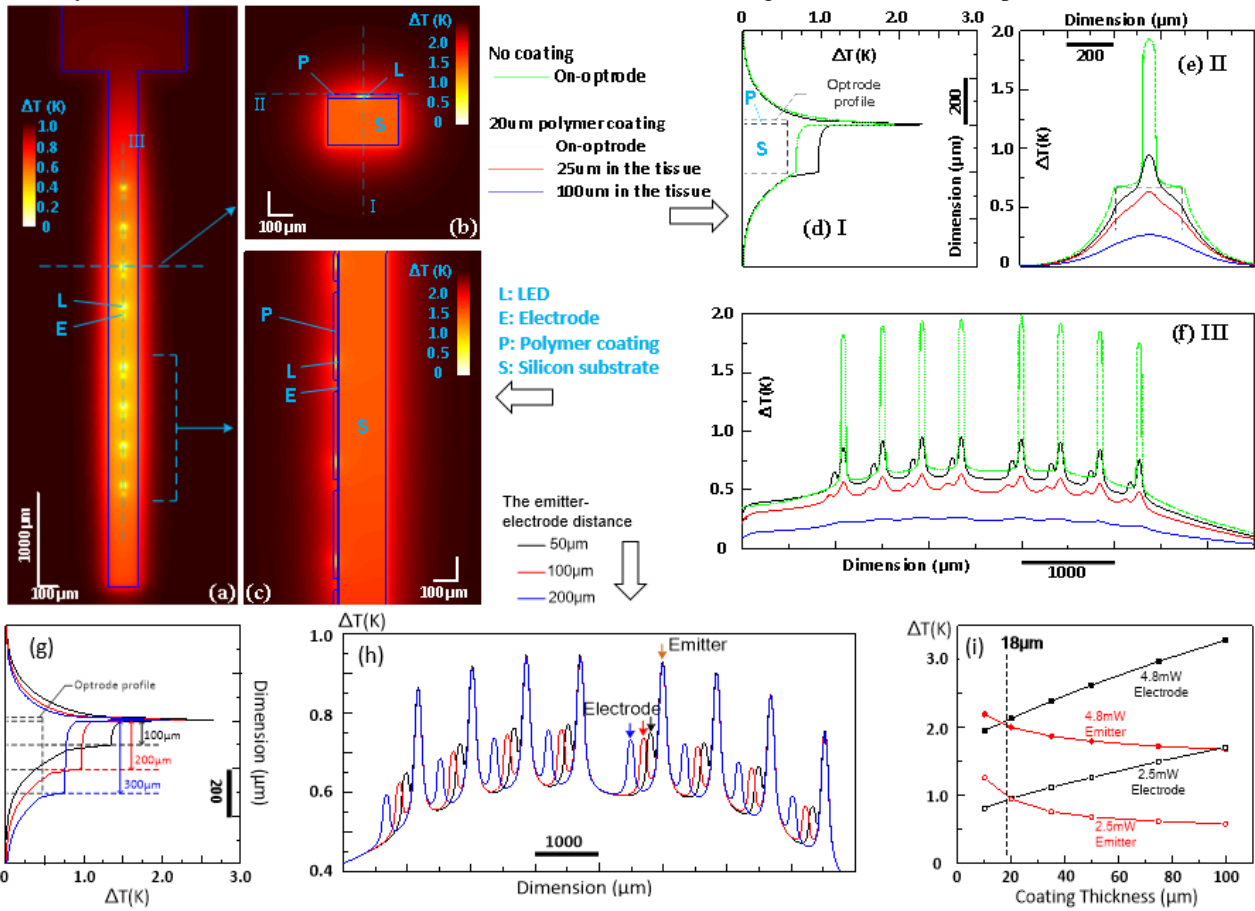


Figure 6 The heat map of the optrode for 100ms CW stimulation. (a) Top view; (b) cross-section; (c) longitudinal section. (d) Temperature distribution along line I for non-encapsulation optrode or optrode with 20 μm encapsulation (e) temperature distribution along line II; (f) temperature distribution along line III. For each LED the total power injected is 2.5mW. (g) Temperature distribution along line I for various substrate heights of 100, 200 and 300 μm . (h) In-tissue temperature distribution along the LED array to show the hot spots for different emitter-electrode distance; (i) Temperature trade-off between the localized hot spots around the emitter and the electrode which is determined by the polymer coating thickness.

and the white background defines the period with the LED off. The x-axis is plotted on a logarithmic time period to show the full range of activity. The y-axis is plotted for both linear (left) and logarithmic (right) time period. The simulation results (red lines) and the experiment results (black lines) are comparable during both the ascent and the decay periods. The experiment was repeated multiple times with similar effect. The data presented is therefore an average for which the quantization error is not as apparent as for (a,b). (c) Represents pulsed stimulus with an LED current of 2.44mA (6.5V LED drive voltage). (d) Represents 7.1mA (15V LED drive voltage) (e) represents (8mA) (7.75V LED drive voltage).

Having built confidence that our model matches the experimental results in air, we utilize the model in water to explore heating effects on the exemplar probe shown in Figure 1 (b) and Table 1. The specific sub-questions we aim to answer are:

- (i) Will uncoated electrodes act as a thermal hotspot?
- (ii) How does the encapsulation affect the surface temperature?
- (iii) How do specific surface hotspots vary with emission intensity?

These questions cannot easily be answered experimentally, particularly in water and thus can benefit from the use of modelling.

Figure 6 (a) to (c) shows a typical result of the modelling for the exemplar optrode, in this case, reaching a steady state for 8 LEDs with a thermal emission of 2.5 mW. Figure 6 (a) is the top-view of the total optrode, (b) and (c) are the cross-section-view and side-section-view at a single LED, respectively.

To answer question (i) the primary hotspots are concentrated around the LED emitters. However, additional spots can be seen at the electrode sites. To see the specific details of the hotspot temperature distribution, we set three lines I, II and III in Figure 6 (a) and (b). Temperature distribution along these three lines is shown in Figure 6 (d) to (f) respectively.

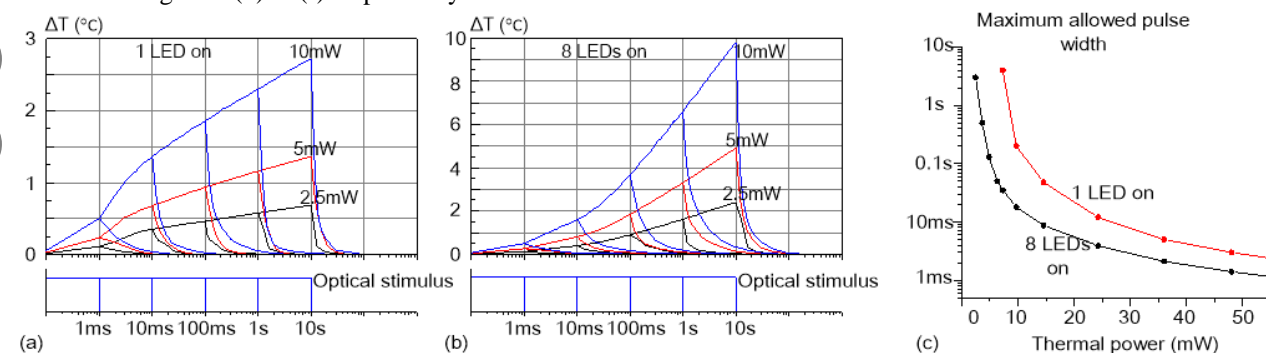


Figure 7 (a,b) Temporal profile of the single pulse ranging from 1ms to 10s for the hottest spot in the tissue for a 1 LED and 8 LEDs respectively. (c) The maximum allowed pulse width and duty cycle for a given thermal power and a temperature increase limit of 2°C.

To answer question (ii): we compare the optrode with or without a 20- μm thick polymer encapsulation. The on-surface temperature distribution of non-passivated optrode is given in the green curves; while for passivated optrode, we present the temperature distribution 0, 25 and 100 μm to the optrode surface in black, red and blue curves respectively. The encapsulation we chose can reduce the hot spot temperature by up to 55% (from 2°C to 0.9°C). The temperature increase falls to about 50% at 25 μm to the optrode surface and about 20% at 100 μm . To explore this further, Figure 6 (g) shows the dependence of the optrode temperature on the thickness of the substrate (100, 200 and 300 μm). Clearly, thicker substrates provide a temporary heat buffer and thus act to distribute the thermal energy, thus reducing hot spots.

Figure 6 (h) shows the dependence of the optrode temperature on the Emitter-electrode distance (50, 100 and 200 μm). There is very little effect with distance from the primary LED heat source. We attribute this to heat traversing along the aluminium wires. Figure 6 (i) shows the dependence of the optrode temperature on the encapsulation coating thickness (10 to 100 μm). Interestingly, beyond 20 μm , the heat from the LEDs begin to primarily escape via the electrodes, thus forming local hot spots at that point.

The final question (iii) centres on the timing of the temperature rise of the maximum local hotspot as a result of the thermal energy pulse transmitted by a μLED . Note, we refer to the hotspot – not the average surface temperature as would be measured by a thermal camera. Figure 7 (a) displays the temperature change for a single LED with the dimensions given in Table 1 and layer thicknesses given in Table 2. Thermal pulses between 1ms and 10s, between 2.5mw and 10mW, are displayed. (b) Shows the same profile if all 8 LEDs are illuminated. Figure 7 (c) Shows the maximum allowed pulse width for a given thermal power and a temperature increase limit of 2°C.

4.2 Optical diffusion in the tissue

Figure 8 (a) shows the extracted light profile taken from Figure 5 (c). Figure 8 (b) shows a quantitative comparison between the experiment profile (lines) and the simulation profile (dots). This demonstrates that for a given emission profile we are broadly able to mimic the transmission profile.

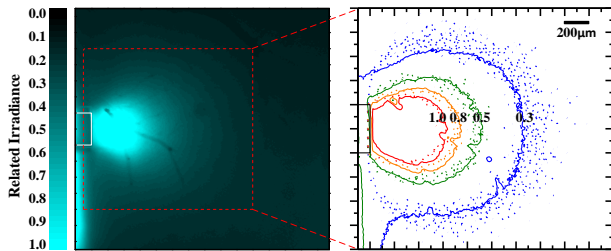


Figure 8: Results show coincidence of the optical modelling and the experiment results. (a) Light penetration experiment photograph from the lateral side. (b) A Quantitative comparison between the experiment profile (lines) and the simulation profile (dots).

It could be argued that there may be some deviation between rodent and human brain due to the differences in cellular density. However, we feel these results demonstrate applicability for both. The results also match previous efforts in the literature such as by Wu et al. (18). With confidence in the model, we can then explore the key sub-questions relating to light penetration into tissue:

- (i) Is it better to have a smaller lower efficiency LED emitting light at a high radiant density or vice versa?
- (ii) What is the effect of light collimation?
- (iii) What is the effective volume of illumination for different types of emitter profile, taking probe gliosis into account?

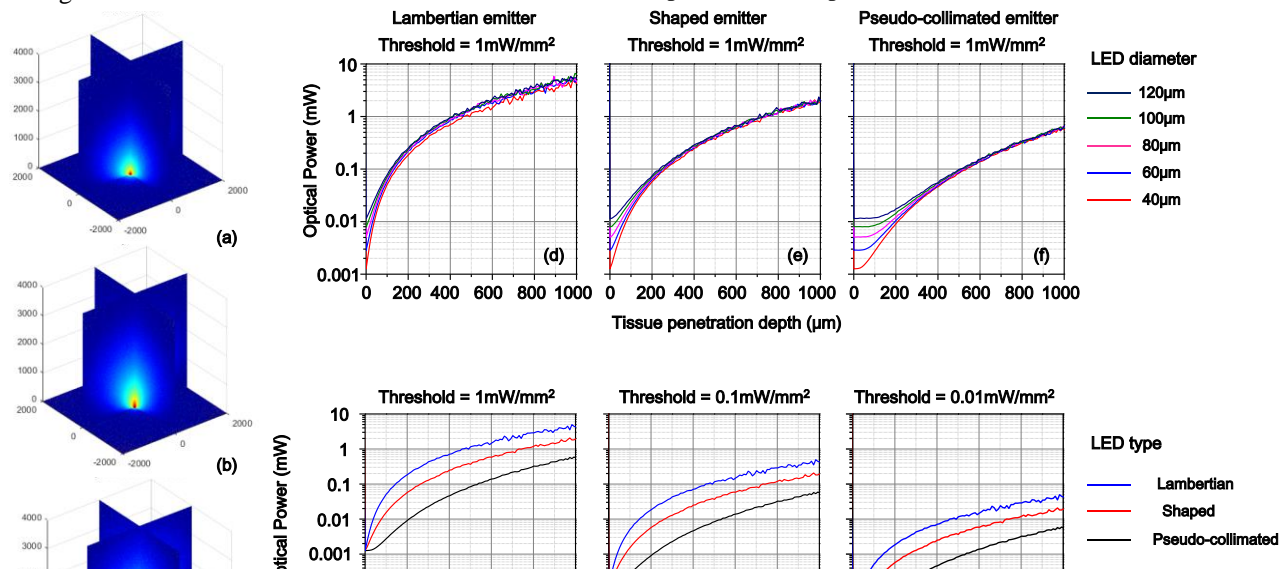


Figure 9: Irradiance profiles of 80µm emitters in a 4mm cube for (a) Lambertian emitter (b) optical-shaped emitter (c) pseudo-collimated emitter (d-i) Optical power versus tissue penetration depth for different thresholds, emitter sizes and emitter types. (a) Lambertian emitter for different sizes at the threshold of 1mW/mm²; (b) optical-shaped emitter for different sizes at the threshold of 1mW/mm²; (c) pseudo-collimated emitter for different sizes at the threshold of 1mW/mm²; (d) Comparison of the three emitter types for emitter diameter = 40µm at the threshold of 1mW/mm²; (e) Comparison of the three emitter types for emitter diameter = 40µm at the threshold of 0.1mW/mm²; (f) Comparison of the three emitter types for emitter diameter = 40µm at the threshold of 0.01mW/mm².

Figure 9 (a) to (c) shows the simulation results of the light penetration profile for Lambertian, optical-shaped and pseudo-collimated emitters respectively. The data in these cases are plotted as the log(normalised intensity). Figure 9 (d) to (f) show the optical power versus penetration depth along the tangential line from the centre of the LED. The penetration depth is defined as the depth which can be attained while still presenting the target irradiance (in this case 1mW/mm²). The plot is shown for each of the different emission profiles and LED diameters from 40 to 120µm.

To answer question (i): Each of the LEDs in Figure 9 (d) to (f) follow the penetration distance for absolute radiance, not radiant density. Thus, for a constant radiant power, the radiant density will increase, and the LED size decreases. However, as can be seen, this only has significance on the penetration depth of a few tens of microns for Lambertian emitters. There is a very limited difference in penetration depth for different sized LEDs with the same absolute radiance. As such, given the droop (efficiency) profile in Figure 2 (a), it is better to use larger LEDs within limits set by the probe dimensions. The caveat is that arrays of pseudo-collimated micro-LEDs, even if not particularly efficient, could be used to individually stimulate local neurons acutely at high resolution, and without crosstalk.

To answer question (ii): Currently, most presented microLEDs have a Lambertian profile, with some having a tighter emission profile which we call here ‘*optical shaped*’. Pseudo-collimated LEDs do not currently exist in the literature for optogenetics. So, it is interesting to predict their relative performance. Figure 9 (g) to (i) show the optical power vs penetration depth for different channelrhodopsin thresholds [1mW/mm², 0.1mW/mm², 0.01mW/mm²]. In addition, even with scattering effects, there is a strong correlation between emitter collimation and penetration depth. As an example, it requires 20mW, 8mW and 1.5mW for Lambertian, optical-shaped and pseudo-collimated emitters respectively to reach a 1mm penetration depth into the tissue at the threshold of

1mW/mm². A further advantage of increasing collimation (not shown here) is reduced crosstalk, which could allow the shown probe scale to high-density stimulation.

Typically, chronically implanted probes will have a tissue reaction whereby there is a zone of glial cells which displace or kill neurons in a region around an implant. From discussions with neuroscientists, such regions of dead neurons can be up to 200μm in depth from the probe. This effectively creates a ‘deadzone’ whereby light stimulus has no impact.

As such, we wanted to explore this question with 3 scenarios: [0, 100, 200] μm of deadzone representing [acute implant, moderate gliosis, severe gliosis]. This concept is described in Figure 10(a).

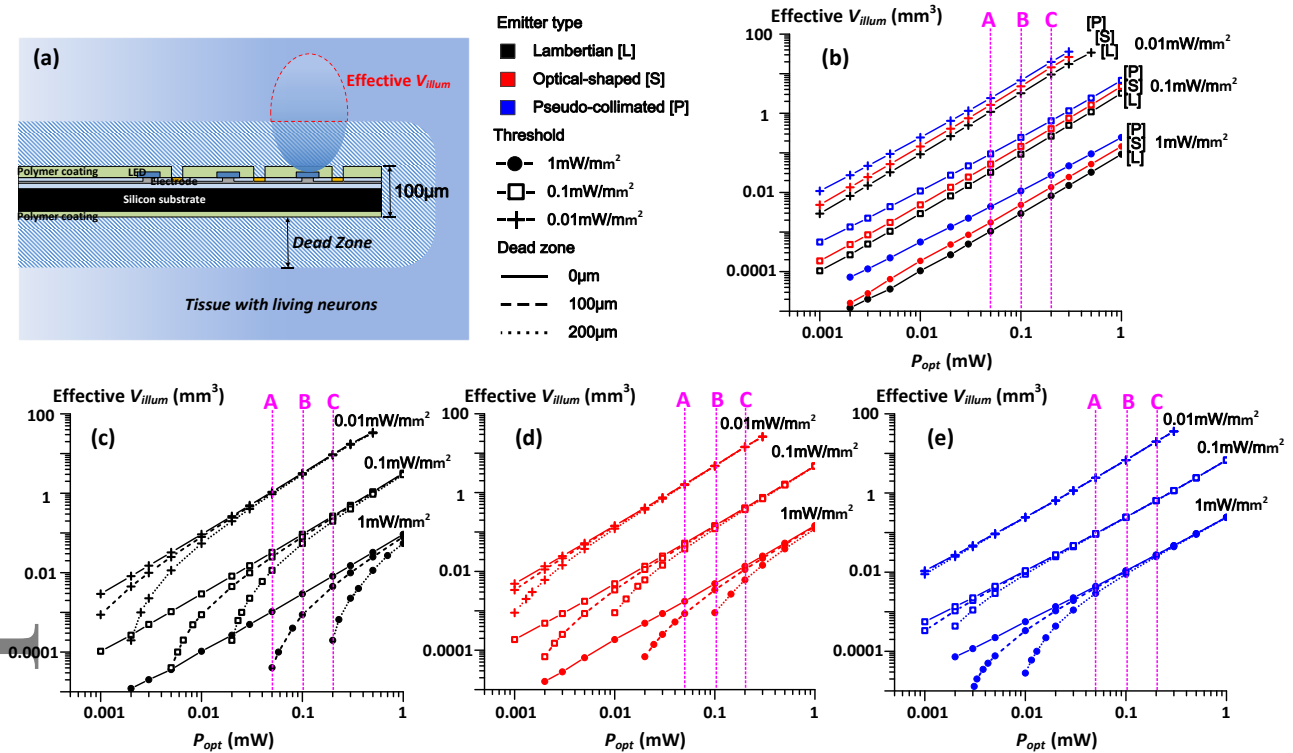


Figure 10: (a) Illustration of the effective illuminated volume in tissue for the given optrode considering dead zone effect; (b) optical power versus effective illuminated volume for different emitter types and thresholds; (c) optical power versus effective illuminated volume for Lambertian emitter, different threshold and dead zones; (d) optical power versus effective illuminated volume for optical-shaped emitter, different threshold and dead zones; (e) optical power versus effective illuminated volume for pseudo-collimated emitter, different threshold and dead zones.

Figure 10 (b) shows the illumination volume as a function of optical power for the acute case. i.e. no deadzone. For comparison, the graphs are plotted for different opsin thresholds and emitter types. The results indicate that there is a slight advantage in illumination volume for more collimated emitters for equal radiance.

Figure 10 (c) to (e) show the effect of deadzone size on illumination volume for different emitter types: Lambertian (c), optical-shaped (d), pseudo-collimated (e). Deadzones of [0, 10, 200] μm are presented, as are the three different possible opsin thresholds of [1, 0.1, 0.01]mW/mm².

From Figure 7, for a typical 10% duty cycle and a stimulus pulse of 100ms. The maximum thermal emission for a single LED is ~ 5.2mW. Under these

conditions. three lines [A, B, C] have been drawn to allow comparison. These represent the maximum optical emission for LED efficiencies of [0.9%, 1.8%, 3.6%] using the relation (16). These efficiencies represent typical efficiencies presented for micro-LEDs in the literature. Corresponding illumination volumes can then be compared for different emitter profiles, channelrhodopsin thresholds and gliosis effects.

4.3 Discussion

A number of important conclusions need to be drawn from this work. First and foremost, are LED-optrodes viable? Clearly, a number of past papers have demonstrated their utility in acute experiments. But what about chronic experiments, where long-term thermal effects and tissue gliosis around the probe become more apparent?

To answer this question, let's consider a typical case of a Lambertian emitter, an opsin threshold of $1\text{mW}/\text{mm}^2$, and a gliosis layer that will eventually surround the probe to a thickness of $200\ \mu\text{m}$. Figure 9 shows that $\sim 0.5\text{mW}$ is required to achieve a penetration threshold of $300\ \mu\text{m}$. i.e. $100\ \mu\text{m}$ of effective penetration beyond the gliosis region. We can then further assume a typical 10% duty cycle and a stimulus pulse of 100ms. From Figure 7, under these conditions, the maximum allowed thermal emission for a single LED is $\sim 5.2\text{mW}$, and for 8 LEDs it is 10.4mW .

We can then relate the optical power requirement with the thermal limit using the following relation, where η_{LED} is the LED efficiency:

$$P_{thermal} = P_{optical} \left(\frac{1 - \eta_{LED}}{\eta_{LED}} \right) \quad (17)$$

The result is that for a single LED optrode, the LED efficiency would need to exceed 4.6%, and for a multiLED optrode, the efficiency would need to exceed 8.5%.

Clearly, with different parameters, these efficiency requirements could be reduced. However, as a general figure of merit, they significantly exceed the optimistic case presented in prior papers. The primary reason for this more pessimistic analysis is that previous work by McAlinden et al. (9) and Wu et al. (18) who did not explore the effects of hotspots or the effects of gliosis.

The caveat to this analysis is that even if a small hotspot forms on the surface – there is a rapid decay with distance from the probe. And such a decay would be presumably through dead tissue. Such consideration would perhaps be acceptable for neuroscience experiments. However, for clinical devices, the current regulations are clear: the surface temperature of the device must not exceed $2\ ^\circ\text{C}$. Though an interesting question is: What is the surface? The encapsulation surface, or gliosis layer? Clearly there is more work to be

done by the These are interesting questions for the community to study in more detail.

The second point to consider is the size of the LED. Figure 9 shows that size has little impact on the irradiance density for a given radiance (in mW). This is certainly the case beyond the $200\ \mu\text{m}$ target discussed above. As such, given the effect of droop shown in Figure 2 and the high efficiency requirement described above, it makes more sense to distribute the light over a larger LED than to utilize smaller LEDs. For example, the commercial miniLED we utilized in our test probe had an efficiency of 30%, compared to only 1-5% for μLEDs . There are two clarifications to this. Firstly, there are applications where high-density optical information transfer is necessary. In such cases, smaller, more collimated emitters are required. Secondly, a cluster of smaller LEDs can have similar aggregate properties as a single larger LED. i.e. for the same total light emission, the overall current density per LED within such a cluster can be low.

The third point to consider is the effect of collimation. All LED-optrodes to date have utilised Lambertian emitters. Our results show that both the penetration depth and penetration volume can be improved with collimation. Importantly, this effect is large when considering the effect of the gliosis deadzone. For a $1\text{mW}/\text{mm}^2$ threshold, a $200\ \mu\text{m}$ deadzone, and an emitter radiance of 0.1mW , a pseudo-collimated emitter will achieve an effective illumination volume of 0.01mm^3 ($10^7\ \mu\text{m}^3$ or $0.2 \times 0.2 \times 0.2\ \text{mm}$), whereas a Lambertian emitter would fail to illuminate any significant volume.

The fourth point relates to encapsulation, which has a low thermal conductivity and thus acts to block heat transmission. This is beneficial, as it acts to spread the heat from a local hot spot around an LED over the whole shaft. However, if too thick, it can result in local hot spots at the next opening – the electrode, which is clearly undesirable. To balance the main μLED hotspot with this secondary electrode hotspot, we find the encapsulation thickness of around $20\ \mu\text{m}$ to be ideal. We do not notice this to be affected considerably by LED – electrode separation.

The final consideration relates to the optrode dimensions. The bulk of the silicon substrate acts as a primary heat-buffer, thus significantly smoothing spikes in heating. As such, a larger shaft is beneficial from a thermal perspective. However, from a tissue interaction perspective, a smaller shaft would be preferable. As such, we attempt to describe such trade-offs in Table 5.

Table 5: Thermal modelling parameters optimization

Optrode dimension (μm)	Variable range	Optimized
Encapsulation thickness	10 – 100	20
Silicon thickness	100-300	200
Emitter diameter	20-200	50

Emitter-electrode distance	50-200	100
μ LED thickness	1-100	1
Head thickness	100-400	200
Shaft width	100-400	300
Shaft thickness	100-400	200

For brevity, we have not considered the effects of circuit heat dissipation on active probes. Such dissipation would typically be in the optrode head and could traverse down the shaft having a small chronic effect on the local temperature. This would need to be considered for high levels of dissipation. However, our recent work with such systems (15, 16) indicates dissipation between 0.1 - 1mW in the head, which for which we would expect a relatively small effect.

As a final note: In this work we have primarily considered the surface temperature of the LEDs. The internal junction temperature will be higher giving rises to questions about effects on longevity. In other work on this topic (17, 55), we have explored such effects which typically amount to 15°C above ambient (i.e. 52°C). This is actually much less than the 80°C operating temperature for lighting LEDs which have operational lifetimes of 20,000 hours

5. Conclusion

We believe this work to be the most detailed study of LED-optrode opto-thermal design to date. It makes a number of conclusions which can be drawn from figures 7-10 and Table 5. For brevity, we will summarise with four primary conclusions:

- (i) Our data suggest that LED-optrodes can viably perform chronic stimulation tissue without excessive heating, as long as they are reasonably efficient. We suggest >4.6% for single LED probes and > 8.5% for multi-LED probes.
- (ii) The size of the LED has little effect on the illumination profile, so given efficiency is a function of current density, it is best to have as large an LED as is viable for a given probe.
- (iii) Collimated emitters are superior to equivalent Lambertian emitters with the same efficiency. This is particularly the case for chronic use where the presence of a 'deadzone' will negate irradiation near to the emitter.
- (iv) We note an optimal encapsulation thickness of around 20 μ m, which balances broad dissipation through the bulk vs local hotspot formation on the electrode.

We believe in the long term, continuous improvements in both μ LED efficiency and the sensitivity of the opsins will improve. But even with the best of today's devices, it is possible with the correct stimulation protocols to

provide optical stimulus without significant tissue heating.

Supporting Information

Additional supporting information may be found in the online version of this article at the publisher's website. Models will be provided freely if requested from the authors.

Acknowledgements Dr Degenaar would like to Acknowledge the European Commission for funding the OptoNeuro project (249867), and the EPSRC and Wellcome Trust for funding the CANDO project (www.cando.ac.uk). Prof. Sun and Mr Dong would like to acknowledge SEU for funding Na Dong's internship.

Author biographies Please see Supporting Information online.

References

1. G. Nagel, T. Szellas, W. Huhn, S. Kateriya, N. Adeishvili, P. Berthold, D. Ollig, P. Hegemann and E. Bamberg, "Channelrhodopsin-2, a directly light-gated cation-selective membrane channel," *Proceedings of the National Academy of Sciences of the United States of America* 100(24), 13940-13945 (2003)
2. X. Han and E. S. Boyden, "Multiple-color optical activation, silencing, and desynchronization of neural activity, with single-spike temporal resolution," *PLoS ONE* 2(3), (2007)
3. V. Busskamp, S. Picaud, J. A. Sahel and B. Roska, "Optogenetic therapy for retinitis pigmentosa," *Gene Therapy* 19(2), 169-175 (2012)
4. A. D. Bi, J. J. Cui, Y. P. Ma, E. Olshevskaya, M. L. Pu, A. M. Dizhoor and Z. H. Pan, "Ectopic expression of a microbial-type rhodopsin restores visual responses in mice with photoreceptor degeneration," *Neuron* 50(1), 23-33 (2006)
5. K. Nikolic, N. Grossman, H. Yan, E. Drakakis, C. Toumazou, P. Degenaar and Ieee, "A non-invasive retinal prosthesis testing the concept," in *2007 Annual International Conference of the Ieee Engineering in Medicine and Biology Society, Vols 1-16*, pp. 6365-+ (2007).
6. A. N. Zorzos, E. S. Boyden and C. G. Fonstad, "Multiwaveguide implantable probe for light delivery to sets of distributed brain targets," *Optics Letters* 35(24), 4133-4135 (2010)
7. H. Cao, L. Gu, S. K. Mohanty and J. C. Chiao, "An Integrated μ LED Optrode for Optogenetic Stimulation and Electrical Recording," *Ieee*

- Transactions on Biomedical Engineering* 60(1), 225-229 (2013)
8. N. Grossman, V. Poher, M. S. Grubb, G. T. Kennedy, K. Nikolic, B. McGovern, R. B. Palmini, Z. Gong, E. M. Drakakis, M. A. A. Neil, M. D. Dawson, J. Burrone and P. Degenaar, "Multi-site optical excitation using ChR2 and micro-LED array," *Journal of Neural Engineering* 7(1), (2010)
 9. N. McAlinden, D. Massoubre, E. Richardson, E. Gu, S. Sakata, M. D. Dawson and K. Mathieson, "Thermal and optical characterization of micro-LED probes for in vivo optogenetic neural stimulation," *Optics Letters* 38(6), 992-994 (2013)
 10. N. Grossman, K. Nikolic, C. Toumazou and P. Degenaar, "Modeling Study of the Light Stimulation of a Neuron Cell With Channelrhodopsin-2 Mutants," *Ieee Transactions on Biomedical Engineering* 58(6), 1742-1751 (2011)
 11. S. Kleinlogel, K. Feldbauer, R. E. Dempsey, H. Fotis, P. G. Wood, C. Bamann and E. Bamberg, "Ultra light-sensitive and fast neuronal activation with the Ca²⁺-permeable channelrhodopsin CatCh," *Nature Neuroscience* 14(4), 513-U152 (2011)
 12. K. Nikolic, N. Grossman, M. S. Grubb, J. Burrone, C. Toumazou and P. Degenaar, "Photocycles of Channelrhodopsin-2," *Photochemistry and Photobiology* 85(1), 400-411 (2009)
 13. P. S. Lagali, D. Balya, G. B. Awatramani, T. A. Munch, D. S. Kim, V. Busskamp, C. L. Cepko and B. Roska, "Light-activated channels targeted to ON bipolar cells restore visual function in retinal degeneration," *Nature Neuroscience* 11(6), 667-675 (2008)
 14. A. Koizumi, K. F. Tanaka and A. Yamanaka, "The manipulation of neural and cellular activities by ectopic expression of melanopsin," *Neuroscience Research* 75(1), 3-5 (2013)
 15. R. Ramezani, Y. Liu, F. Dekhoda, A. Soltan, D. Haci, H. Zhao, T. Constandinou and P. Degenaar, "A microelectronic control system for closed-loop optoelectronic neural interfaces " *IEEE Transactions on Biomedical Circuits and Systems* In review((2017)
 16. H. Zhao, A. Soltan and P. Degenaar, "A Scalable Optoelectronic Neural Probe Architecture with Self-Diagnostic Capability," *IEEE Transactions on Circuits and systems - I* in review(
 17. A. Soltan, B. McGovern, E. Drakakis, M. Neil, P. Maaskant, M. Akhter, J. S. Lee and P. Degenaar, "High Density, High Radiance micro-LED Matrix for Optogenetic Retinal Prostheses and Planar Neural Stimulation," *Ieee Transactions on Biomedical Circuits and Systems* 11(2), 347-359 (2017)
 18. F. Wu, E. Stark, P. C. Ku, K. D. Wise, G. Buzsaki and E. Yoon, "Monolithically Integrated mu LEDs on Silicon Neural Probes for High-Resolution Optogenetic Studies in Behaving Animals," *Neuron* 88(6), 1136-1148 (2015)
 19. Y. Narukawa, M. Ichikawa, D. Sanga, M. Sano and T. Mukai, "White light emitting diodes with super-high luminous efficacy," *Journal of Physics D-Applied Physics* 43(35), (2010)
 20. A. Bhandari, B. Hamre, Ø. Frette, K. Stamnes and J. J. Stamnes, "Modeling optical properties of human skin using Mie theory for particles with different size distributions and refractive indices," *Optics Express* 19(15), 14549-14567 (2011)
 21. C. F. Bohren and D. R. Huffman, "Absorption and scattering of light by small particles," pp. xiv, 530 p.-xiv, 530 p. (1983).
 22. J. C. Lamanna, K. A. McCracken, M. Patil and O. J. Prohaska, "Stimulus-Activated changes in brain-tissue temperature in the anaesthetized rat," *Metabolic Brain Disease* 4(4), 225-237 (1989)
 23. S. Kim, P. Tathireddy, R. A. Normann and F. Solzbacher, "Thermal impact of an active 3-D microelectrode array implanted in the brain," *Ieee Transactions on Neural Systems and Rehabilitation Engineering* 15(4), 493-501 (2007)
 24. N. Matsumi, K. Matsumoto, N. Mishima, E. Moriyama, T. Furuta, A. Nishimoto and K. Taguchi, "Thermal Damage Threshold of Brain Tissue - Histological Study of Heated Normal Monke&y mBrdaaisnhs," *Neurol Med Chir (Tokyo)* 34(209-215 (1994)
 25. T. Fujii and Y. Ibata, "Effects of heating on electrical-activities of guinea-pig olfactory cortical slices," *Pflugers Archiv-European Journal of Physiology* 392(3), 257-260 (1982)
 26. N. L. Opie, U. Greferath, K. A. Vessey, A. N. Burkitt, H. Meffin, D. B. Grayden and E. L. Fletcher, "Retinal Prosthesis Safety: Alterations in Microglia Morphology due to Thermal Damage and Retinal Implant Contact," *Investigative Ophthalmology & Visual Science* 53(12), 7802-7812 (2012)
 27. L. S. Goldstein, M. W. Dewhirst, M. Repacholi and L. Kheifets, "Summary, conclusions and recommendations: adverse temperature levels in the human body," *International Journal of Hyperthermia* 19(3), 373-384 (2003)
 28. T. M. Seese, H. Harasaki, G. M. Saidel and C. R. Davies, "Characterization of tissue morphology, angiogenesis, and temperature in the adaptive response of muscle tissue to chronic heating," *Laboratory Investigation* 78(12), 1553-1562 (1998)
 29. Y. Okazaki, C. R. Davies, T. Matsuyoshi, K. Fukamachi, K. E. Wika and H. Harasaki, "Heat from an implanted power source is mainly dissipated by blood perfusion," *Asaio Journal* 43(5), M585-M588 (1997)
 30. J. M. Stujenske, T. Spellman and J. A. Gordon, "Modeling the Spatiotemporal Dynamics of Light

- and Heat Propagation for In Vivo Optogenetics," *Cell Reports* 12(3), 525-534 (2015)
31. H. H. Pennes, "Analysis of tissue and arterial blood temperatures in the resting human forearm," *Journal of applied physiology* 1(2), 93-122 (1948)
 32. J. G. Du, T. J. Blanche, R. R. Harrison, H. A. Lester and S. C. Masmanidis, "Multiplexed, High Density Electrophysiology with Nanofabricated Neural Probes," *Plos One* 6(10), (2011)
 33. C. von Economo and L. C. Triarhou, *Atlas of Cytoarchitectonics of the Adult Human Cerebral Cortex*, Karger (2008).
 34. C. M. Lopez, A. Andrei, S. Mitra, M. Welkenhuysen, W. Eberle, C. Bartic, R. Puers, R. F. Yazicioglu and G. G. E. Gielen, "An Implantable 455-Active-Electrode 52-Channel CMOS Neural Probe," *Ieee Journal of Solid-State Circuits* 49(1), 248-261 (2014)
 35. G. N. Angotzi, M. Malerba, S. Zucca, L. Berdondini and Ieee, "A 512-channels, whole array readout, CMOS implantable probe for acute recordings from the brain," in *2015 37th Annual International Conference of the Ieee Engineering in Medicine and Biology Society*, pp. 877-880 (2015).
 36. Cree Corp, "Direct Attach DA2432™ LEDs - Data Sheet CxxxDA2432-Sxxx00-2," (2016).
 37. A. Bejan, *Convection Heat Transfer*, Wiley (2013).
 38. M. Kurihara and Y. Sudo, "Microbial rhodopsins: wide distribution, rich diversity and great potential," *Biophysics and Physicobiology* 12(121-129) (2015)
 39. J. Iveland, L. Martinelli, J. Peretti, J. S. Speck and C. Weisbuch, "Direct Measurement of Auger Electrons Emitted from a Semiconductor Light-Emitting Diode under Electrical Injection: Identification of the Dominant Mechanism for Efficiency Droop," *Physical Review Letters* 110(17), (2013)
 40. P. P. Maaskant, H. Shams, M. Akhter, W. Henry, M. J. Kappers, D. Zhu, C. J. Humphreys and B. Corbett, "High-Speed Substrate-Emitting Micro-Light-Emitting Diodes for Applications Requiring High Radiance," *Applied Physics Express* 6(2), (2013)
 41. L. Chaudet, M. Neil, P. Degenaar, K. Mehran, R. Berlinguer-Palmini, B. Corbet, P. Maaskant, D. Rogerson, P. Lanigan, E. Bamberg, B. Roska, S. K. Mohanty and N. V. Thakor, "Development of Optics with Micro-LED Arrays for Improved Optoelectronic Neural Stimulation," *Optogenetics: Optical Methods For Cellular Control* 8586(1-7) (2013)
 42. L. V. Wang, S. L. Jacques and L. Zheng, "MCML - Monte Carlo modeling of light transport in multi-layered tissues," *Computer Methods and Programs in Biomedicine* 47(1995), 131-146 (1995)
 43. A. N. Yaroslavsky, P. C. Schulze, I. V. Yaroslavsky, R. Schober, F. Ulrich and H. J. Schwarzman, "Optical properties of selected native and coagulated human brain tissues in vitro in the visible and near infrared spectral range," *Physics in medicine and biology* 47(12), 2059-2073 (2002)
 44. R. Drezek, A. Dunn and R. Richards-Kortum, "Light scattering from cells: finite-difference time-domain simulations and goniometric measurements," *Applied optics* 38(16), 3651-3661 (1999)
 45. Y. L. Jin, J. Y. Chen, L. Xu and P. N. Wang, "Refractive index measurement for biomaterial samples by total internal reflection," *Physics in medicine and biology* 51(N371-N379) (2006)
 46. B. Bilenberg, T. Nielsen, B. Clausen and A. Kristensen, "PMMA to SU-8 bonding for polymer based lab-on-a-chip systems with integrated optics," *Journal of Micromechanics and Microengineering* 14(6), 814-818 (2004)
 47. D. A. Chang-Yen, R. K. Eich and B. K. Gale, "A monolithic PDMS waveguide system fabricated using soft-lithography techniques," *Journal of Lightwave Technology* 23(6), 2088-2093 (2005)
 48. M. E. Thomas, S. K. Andersson, R. M. Sova and R. I. Joseph, "Frequency and temperature dependence of the refractive index of sapphire," *Infrared Physics & Technology* 39(4), 235-249 (1998)
 49. S. Pezzagna, J. Brault, M. Leroux, J. Massies and M. de Micheli, "Refractive indices and elasto-optic coefficients of GaN studied by optical waveguiding," *Journal of Applied Physics* 103(12), (2008)
 50. D. R. H. Craig F. Bohren, *Absorption and scattering of light by small particles*, Wiley (1998).
 51. A. Taddeucci, F. Martelli, M. Barilli, M. Ferrari and G. Zaccanti, "Optical properties of brain tissue," *BIOMEDO* 1(1), 117-123 (1996)
 52. D. A. Sun, H. Yu, J. Spooner, A. D. Tatsas, T. Davis, T. W. Abel, C. Kao and P. E. Konrad, "Postmortem analysis following 71 months of deep brain stimulation of the subthalamic nucleus for Parkinson disease," *Journal of neurosurgery* 109(2), 325-329 (2008)
 53. D. H. Szarowski, M. D. Andersen, S. Retterer, A. J. Spence, M. Isaacson, H. G. Craighead, J. N. Turner and W. Shain, "Brain responses to micro-machined silicon devices," *Brain research* 983(1-2), 23-35 (2003)
 54. R. W. Griffith and D. R. Humphrey, "Long-term gliosis around chronically implanted platinum electrodes in the Rhesus macaque motor cortex," *Neuroscience letters* 406(1-2), 81-86 (2006)
 55. F. Dehkoda, A. Soltan, N. Ponor, A. Jackson, A. O'Neill and P. Degenaar, "Self-sensing of temperature rises on light emitting diode based optodes," *Journal of Neural Engineering* 15(2), (2018)